ARL-TR-8675 • MAR 2019

DEVCOM ARMY RESEARCH LABORATORY

The Compressive Mechanical Response of the Human Skull: Implementation of Morphology-Based Mechanical Deformation Model in a 3-D Finite-Element Simulation

by Stephen L Alexander, C Allan Gunnarsson, and Tusit Weerasooriya

NOTICES

Disclaimers

The research reported in this document was performed in connection with contract/instrument W911QX-16-D-0014 with the US Army Research Laboratory. (As of 31 January 2019, the organization is now part of the US Army Combat Capabilities Development Command [formerly RDECOM] and is now called CCDC Army Research Laboratory.)

The findings in this report are not to be construed as an official Department of the Army position unless so designated by other authorized documents.

Destroy this report when it is no longer needed. Do not return it to the originator.

ARL-TR-8675 ● MAR 2019

The Compressive Mechanical Response of the Human Skull: Implementation of Morphology-Based Mechanical Deformation Model in a 3-D Finite-Element Simulation

by Stephen L Alexander
SURVICE Engineering Company

C Allan Gunnarsson and Tusit Weerasooriya
Weapons and Materials Research Directorate, CCDC Army Research Laboratory

REPORT DOCUMENTATION PAGE

Form Approved
OMB No. 0704-0188

1. REPORT DATE *(DD-MM-YYYY)*	2. REPORT TYPE	3. DATES COVERED (From - To)
March 2019	Technical Report	February–December 2018

4. TITLE AND SUBTITLE
The Compressive Mechanical Response of the Human Skull: Implementation of Morphology-Based Mechanical Deformation Model in a 3-D Finite-Element Simulation

5a. CONTRACT NUMBER
W911QX-16-D-0014

5b. GRANT NUMBER

5c. PROGRAM ELEMENT NUMBER

6. AUTHOR(S)
Stephen L Alexander, C Allan Gunnarsson, and Tusit Weerasooriya

5d. PROJECT NUMBER

5e. TASK NUMBER

5f. WORK UNIT NUMBER

7. PERFORMING ORGANIZATION NAME(S) AND ADDRESS(ES)
US Army Combat Capabilities Development Command, Army Research Laboratory; ATTN: FCDD-RLW-PB
Aberdeen Proving Ground, MD 21005-5069

8. PERFORMING ORGANIZATION REPORT NUMBER
ARL-TR-8675

9. SPONSORING/MONITORING AGENCY NAME(S) AND ADDRESS(ES)

10. SPONSOR/MONITOR'S ACRONYM(S)

11. SPONSOR/MONITOR'S REPORT NUMBER(S)

12. DISTRIBUTION/AVAILABILITY STATEMENT
Approved for public release; distribution is unlimited.

13. SUPPLEMENTARY NOTES
The work outlined in this report was performed while the US Army Research Laboratory was part of the US Army Research, Development, and Engineering Command (RDECOM). As of 31 January 2019, the organization is now part of the US Army Combat Capabilities Development Command (formerly RDECOM) and is now called CCDC Army Research Laboratory.

ORCID ID: Tusit Weerasooriya, 0000-0003-3299-2166

14. ABSTRACT

A power law relating the compressive initial modulus of adult human skull to the microstructure, specifically the bone volume fraction (BVF), was published in 2018 at the US Army Research Laboratory. In this current study, using the microstructurally inspired modulus relationship, a finite-element computational concept was developed to obtain the mechanical response of a skull coupon structure during compression. Using the local moduli of each element obtained from the power law with the measured local BVF, the ability to simulate a fully instrumented quasi-static compression experiment of a 3-D skull bone coupon was evaluated. Instead of explicitly meshing the internal porous microstructure, a simplistic mesh was used that was bounded by the outer geometry of the specimen. Therefore, elements represented both bone and pores, and a method was developed to calculate the BVF of the physical volume each element represented. Then, each element was assigned mechanical properties using the modulus–BVF relationship. The ability of the power-law-relationship-based simulation to replicate the experimentally measured linear stiffness and full-field surface strains was confirmed. This proposed procedure allows efficient computational simulation of mechanical loading of material with complex biological microstructures while also bridging the length scales from complex microstructural scale to meso-scale.

15. SUBJECT TERMS
human-head simulation, compression human skull, modulus human skull, human-skull morphology, microcomputed tomography, micro-CT-based mesh, micro finite element, digital image correlation

16. SECURITY CLASSIFICATION OF:			17. LIMITATION OF ABSTRACT	18. NUMBER OF PAGES	19a. NAME OF RESPONSIBLE PERSON
a. REPORT	b. ABSTRACT	c. THIS PAGE			Stephen L Alexander
Unclassified	Unclassified	Unclassified	UU	28	19b. TELEPHONE NUMBER (Include area code) 410-306-0917

Contents

List of Figures

Acknowledgments

The authors would like to acknowledge the contributions of several researchers at the US Army Research Laboratory: P Justin McKee for the Python script used to create the Abaqus input file, as well as Brian Fagan and Brian Powers for technical guidance with Abaqus and High Performance Computing.

1. Introduction

At the US Army Combat Capabilities Development Command Army Research Laboratory (CCDC ARL), computer simulations that are conducted to evaluate the head protection of warfighters rely on accurate material models of the response of the skull to mechanical loading. However, there is only a sparse set of experimental data available describing the mechanical properties of skull bones, in particular. Mechanical properties obtained from other bones cannot be used to describe the skull a priori because different bones have different microstructural details affecting the apparent mechanical response of these bones (Morgan and Keaveny 2001, Morgan et al. 2003). The porosity of adult human skull bone varies through the thickness of the skull, from the inner surface nearest to the brain to the outer surface nearest to the skin. This thickness variation can be represented with a Gaussian function and as a sandwich structure with 30% porosity thresholds separating each layer (Alexander et al. 2019). The outer and inner layers, the outer and inner tables, comprise relatively dense cortical bone and enclose a highly porous middle layer called the diploe. The thicknesses and porosities of the three layers differ between the skull bone at the front of the head (frontal bone) and those on the sides (parietal bones), as previously documented (Alexander et al. 2019).

The mechanical properties of bone have a strong dependence on the bone volume fraction (BVF). For example, relationships are well established for the BVF dependence of the tensile elastic modulus and failure strength (e.g., Boruah et al. 2017), yield stresses and strains (e.g., Mirzaali et al. 2016), and fracture toughness (Cook and Zioupos 2009). Similarly, a recent ARL* report documented a power-law relationship between the BVF and the initial modulus of the human skull (Alexander et al. 2018). The power law was derived from using uniaxial compression experiments, with full-field strain measurement using digital image correlation (DIC) on two outer surfaces. These experiments were performed on specimens from both frontal and parietal bones containing the entire thickness of the skull with all three layers of the sandwich structure. The power-law relationship was used to calculate the normalized depth-dependent mechanical properties of the human skull, thus providing an updated data set for use in human-skull simulations.

The approximations and assumptions used in deriving the power-law relationship from the compression experiments remained to be validated through a

*The work outlined in this report was performed while the US Army Research Laboratory (ARL) was part of the US Army Research, Development, and Engineering Command (RDECOM). As of 31 January 2019, the organization is now part of the US Army Combat Capabilities Development Command (formerly RDECOM) and is now called CCDC Army Research Laboratory.

finite-element (FE) simulation of the mechanical response of the full 3-D specimen in the experiment. A direct way of simulating the experiment would be to construct a biofidelic mesh of the porous bone microstructure. The elements of this mesh would represent the bone portion of the specimen. Therefore, all of the elements would be assigned the material properties corresponding to pure bone (BVF = 1). However, the complex microstructure would make building a biofidelic mesh for the human skull particularly challenging, requiring considerable effort and likely millions of elements. These challenges had been previously demonstrated in the case of the adolescent minipig skull (Fagan 2017). For example, Fagan created biofidelic meshes in order to model a coupon of porcine skull bone. Although the coupon measured only 5 mm × 5 mm × 3 mm, the original mesh of this volume consisted of more than 6 million elements. This mesh was abandoned in favor of modeling only representative volumes due to reduced computational expense and in order to better capture the complex geometry of the microstructure.

A more readily achievable simulation method would be to account for the mechanical heterogeneity arising from the bones and pores by assigning unique mechanical properties to elements based on the BVF of the physical volume of the actual specimen each element represents. This approach removes the need for the geometry of the mesh to conform to the bone microstructure. Researchers have used such methods of element-specific material property assignment in order to simulate different bones such as the femur (e.g., Bessho et al. 2007, Taddei et al. 2007, and Zhang et al. 2015) and vertebrae (e.g., Brown et al. 2017). In these studies, mechanical properties were assigned by mapping the mesh to the microcomputed-tomography (micro-CT) data set either through commercial software such as Mimics (Zhang et al. 2015) or Simpleware (Brown et al. 2014), open-source software such as BoneMat (Taddei et al. 2007), or other researcher-developed methods (Bessho et al. 2007).

In this paper, the previously published power-law relationship between the human skull modulus and BVF was implemented in a micro-CT-based FE simulation. The model was of a quasi-static compression experiment performed on a through-thickness skull coupon containing the entire sandwich structure. A custom method was developed to individually assign mechanical properties to the elements based on the BVF of the volume of the specimen they represented. The ability of the power-law relationship to model the experiment was then analyzed. The linear portion of the experimental load-displacement curve was compared with the simulation. Furthermore, the 2-D strain fields measured experimentally through use of DIC were compared with the full-field strain obtained from the simulation. The simulation demonstrated that the power-law relationship combined with a

micro-CT-based meshing technique was able to match the linear portion of the compression response of the human skull.

2. Methods

2.1 Specimen Extraction

A through-thickness specimen was extracted from the frontal bone of a postmortem human subject, age 79 years. The extraction procedures and donor information were previously reported in full (Alexander et al. 2019), where the specimen used in this report was labeled as Specimen 04-09. A pathology bone saw (Exakt 312) under constant irrigation was used to extract the specimen from the skull. The specimen measured 8 mm × 8 mm on the outer surface and was removed with the outer and inner surfaces left intact. The outer surface will refer to the surface nearest to the skin, while the inner surface will refer to the surface nearest to the brain. The outer and inner surfaces will also be referenced in this report as the top and bottom, respectively. After extraction, the specimen was wet-sanded such that the top and bottom surfaces were flat and parallel. The specimen was submersed in Hank's Balanced Salt Solution and stored at 4 °C when not undergoing mechanical or morphological characterization.

2.2 Morphological Characterization and Compression Experiment

Details regarding morphological characterization and the quasi-static compression experimentation have been previously documented (Alexander et al. 2018). Briefly, the specimen was imaged with a desktop micro-CT system (Skyscan 1172, Bruker micro-CT) with an isotropic voxel resolution of 1 voxel = 5.3 microns. Figure 1 shows a 3-D representation of the micro-CT images. The dimension spanning from the inner surface to the outer surface will be referred to in this report as the depth, thickness, or y-dimension. The x–z plane will be referred to as the orthogonal plane, as it was perpendicular to the y-dimension. The orthogonal plane was also approximately the plane of the outer surface. After postprocessing, the specimen was represented digitally as a stack (series) of roughly 2000 cross-sectional images. These cross-sectional images were in the orthogonal plane and were separated from each other along the depth dimension by a thickness equal to the isotropic voxel size. Figure 1 includes an example of a cross-sectional image.

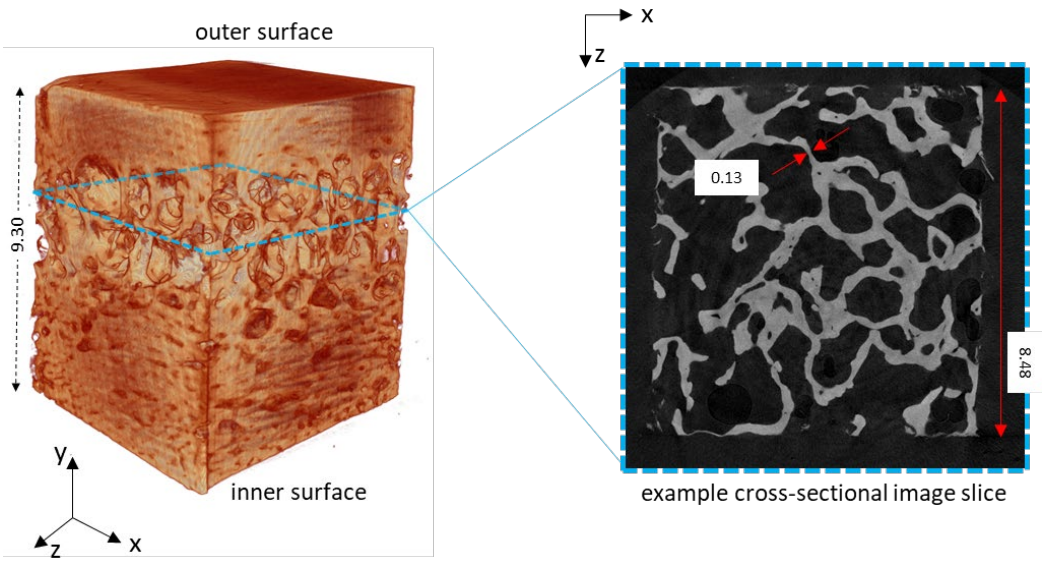

Fig. 1 3-D representation of the micro-CT image set (left) with an example cross-sectional image (right, not at same scale) taken from the diploe; dimensions in mm

The specimen was compressed in the depth dimension by a servo-hydraulic loading frame (Instron 1331 with a 5000-lb load cell) in contact with the sanded outer and inner surfaces of the specimen. Loading was displacement-controlled to achieve a nominal strain rate of 0.001/s. Speckle patterns were applied to the compression platens of the loading frame in order to use DIC to track the relative movement between the two platens directly in contact with the specimen. DIC tracking of the platen movement provided a more accurate method of obtaining the displacement applied to the specimen as compared with the displacement output from the Instron loading machine, since the latter included the machine compliance (documented in Alexander et al. 2018).

The four free, nonloaded sides of the specimen will be referred to as the specimen faces. The faces included the entire thickness dimension, from the outer to inner surfaces. Prior to loading the specimens, two adjacent faces (joined by a single edge) were also speckled to obtain full strain fields using DIC. Two cameras were used to capture the deformation of the two adjacent speckled faces during deformation. One camera was focused on the left face (referred to as the left camera), and the other camera was focused on the right face (referred to as the right camera). The images of the speckle patterns were post-processed using VIC-2D (Correlated Solutions, Inc.) to obtain displacement and strain fields.

As previously reported, the specimen showed three loading phases: a loading phase during which the force reached a local maximum, followed by failure of the highly porous diploe, and finally reloading of the crushed specimen. The present report focuses only on the first loading phase, shown in Fig. 2. The load measured from

the load cell, L, is plotted as a function of applied displacement, δ, calculated from DIC of the images of the moving platen. The platen displacement was averaged from the results of the left and right cameras, although the differences were minimal.

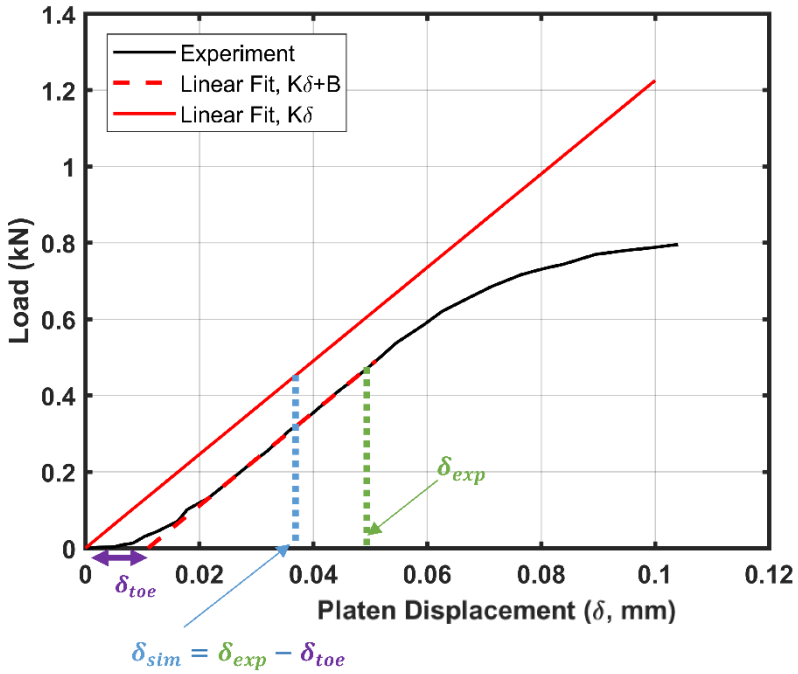

Fig. 2 Experimental load-displacement curve from first loading phase of Specimen 04-09 (shown as black curve); time point of comparison between experiment and simulation is marked as δ_{exp} and δ_{sim} respectively, and linear fit parameters were K = 12.25 kN/mm and B = –0.13 kN

The time point in the experiment corresponding to an applied displacement of $\delta_{exp} = 0.05$ mm was chosen to compare with the simulation, since the experimental load-displacement curve was linear at this point (see Fig. 2). The experimental loading curve showed an initial toe region, which was identified to arise from experimental artifacts such as uneven specimen-loading surfaces (Alexander et al. 2018). The amount of displacement in the simulation, δ_{sim}, which would correspond with δ_{exp} was calculated by accounting for the amount of displacement in the toe region, δ_{toe}. First, the relationship between load (L) and displacement (δ) in the linear portion of the load-displacement curve was described as $L = K\delta + B$. The parameter K corresponded to the stiffness and was measured as K=12.25kN/mm, and the parameter B was –0.13kN. This linear fit was then used to calculate the toe displacement: $\delta_{toe} = -B/K = 1.1 \times 10^{-2}$mm.

2.3 Mesh Generation

A mesh in the form of a rectangular parallelepiped was generated as a first-order approximation of the true 3-D shape of the specimen. First, the images were resampled at a factor of 16, downsizing the data set to a resolution of 1 voxel = 85 microns so as to discard noise and smaller pores while preserving only large macroscopic features. Next, a volume of interest (VOI) in the form of a rectangular parallelepiped was identified using CTAn software (Bruker microCT) and will be referred to as the rectangular VOI. The rectangular VOI was made as large as possible so as to contain as much of the specimen as could fit within a rectangular geometry. It consisted of 110 cross-sectional images of the orthogonal (x–z) plane, where each image was 82 × 69 pixels. The images of the rectangular VOI were then binarized using an automated method (Otsu 1975). After binarization, each x,z pixel of the images had a value, I_{xz}, that was either $I_{xz} = 255$ (white), corresponding to bone, or $I_{xz} = 0$ (black), corresponding to porous space.

A voxel-based stereo-lithography (STL) file was produced of the outer perimeter of the rectangular VOI. The STL was then imported into Hypermesh software, where a volumetric mesh was created with 16,683 tetrahedral elements filling the volume of the rectangular parallelepiped. The average element volume was 13,488 $\mu m^3 \pm 8{,}099\ \mu m^3$.

2.4 Material-Property Assignment

Linear elastic material properties were assigned to each element based on the bone volume fraction, f_{BV}, within the specific volume of the micro-CT data set to which the element corresponded. Each pixel (x,z) of the micro-CT images (y) directly corresponded to an (x,y,z) point within the volumetric mesh because the volumetric mesh was based on the voxel coordinate system of the micro-CT data set. Therefore, the BVF of each element, f_{BV}^{n}, was calculated by iterating through all of the pixels of the micro-CT data set and identifying which element contained each pixel.

The iterative procedure of mapping micro-CT pixels to mesh elements was executed within MATLAB. First, the volumetric mesh was recreated in the MATLAB environment by instantiating a *triangulation* object, *TR*, based on the nodal connectivity and nodal coordinates of the volumetric mesh. Then, each element, *n*, was assigned an array $\mathbf{F}^n$, which would contain the values of each of the pixels (I_{xz}) that lay within the volume of the element.

The **F** arrays were populated in the following manner. Each of the 110 cross-sectional images was sequentially loaded from the resized and binarized VOI

data set into MATLAB using the *imread* function. As a result, each cross-sectional image was represented as a matrix, $\mathbf{M}_{ij}$, which held the values of the image pixels ($\mathbf{I}_{xz}$). Therefore, each matrix entry (i,j) corresponded to an image pixel (x,z) and contained either the numerical value $\mathbf{M}_{ij} = 255$ (bone) or $\mathbf{M}_{ij} = 0$ (porous space). Then, for each matrix entry, the *pointLocation* function of MATLAB was used to identify the mesh element containing the particular (x,y,z) coordinates of the pixel. The matrix entry value ($\mathbf{M}_{ij}$) was then stored in the **F** array of the element. This procedure was repeated for each pixel of each cross-sectional image.

After all of the images were analyzed, the average BVF of each element *n*, f_{BV}^{n}, was calculated from its **F** array:

$$f_{BV}^{n} = \frac{mean(\mathbf{F}^{n})}{255}. \quad (1)$$

Therefore, f_{BV}^{n} ranged from $f_{BV}^{n} = 0$, for elements containing no bone, to $f_{BV}^{n} = 1$, for elements containing only bone without pores. Next, the element BVF values were rounded to the nearest 0.01 so as to limit the number of different materials used in the simulation to 101. Finally, values of $f_{BV}^{n} = 0.00$ were approximated as $f_{BV}^{n} = 0.0001$ so as to yield nonzero mechanical properties in order to avoid numerical instability. Figure 3 shows the f_{BV}^{n} distribution among the elements.

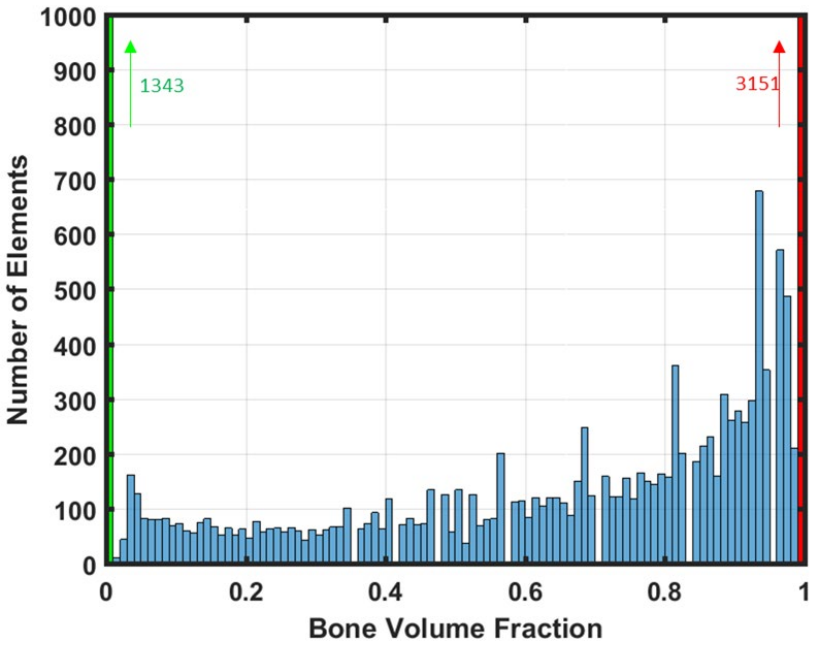

Fig. 3 Number of elements assigned to each BVF value (f_{BV}^{n}), totaling 16,683; number of elements with $f_{BV}^{n} = 0.0001$ was 1,343 (green bar) and number of elements with $f_{BV}^{n} = 1.00$ was 3,151 (red bar)

The Poisson's ratio was assumed to be 0.3 for all elements. The density of each element, ρ^n, was calculated by scaling the density of pure bone, assumed to be 1.8g/cm^3, by the BVF:

$$\rho^n = 1.8(f_{BV}^n). \quad (2)$$

The modulus of each element, E^n, was calculated using the modulus–BVF relationship developed at ARL for skull-bone mechanical properties (Alexander et al. 2018):

$$E^n = 8.755(f_{BV}^n)^{1.603}. \quad (3)$$

A custom-written Python script was used to create an Abaqus input file (.inp), using the mesh nodal connectivity and coordinates, together with the mechanical properties of each element (Poisson's ratio, density, and elastic modulus). This preliminary input file contained mesh details and material property assignments for each of the 101 different blocks of elements. Figure 4 shows the mesh with details of the BVF and modulus distributions.

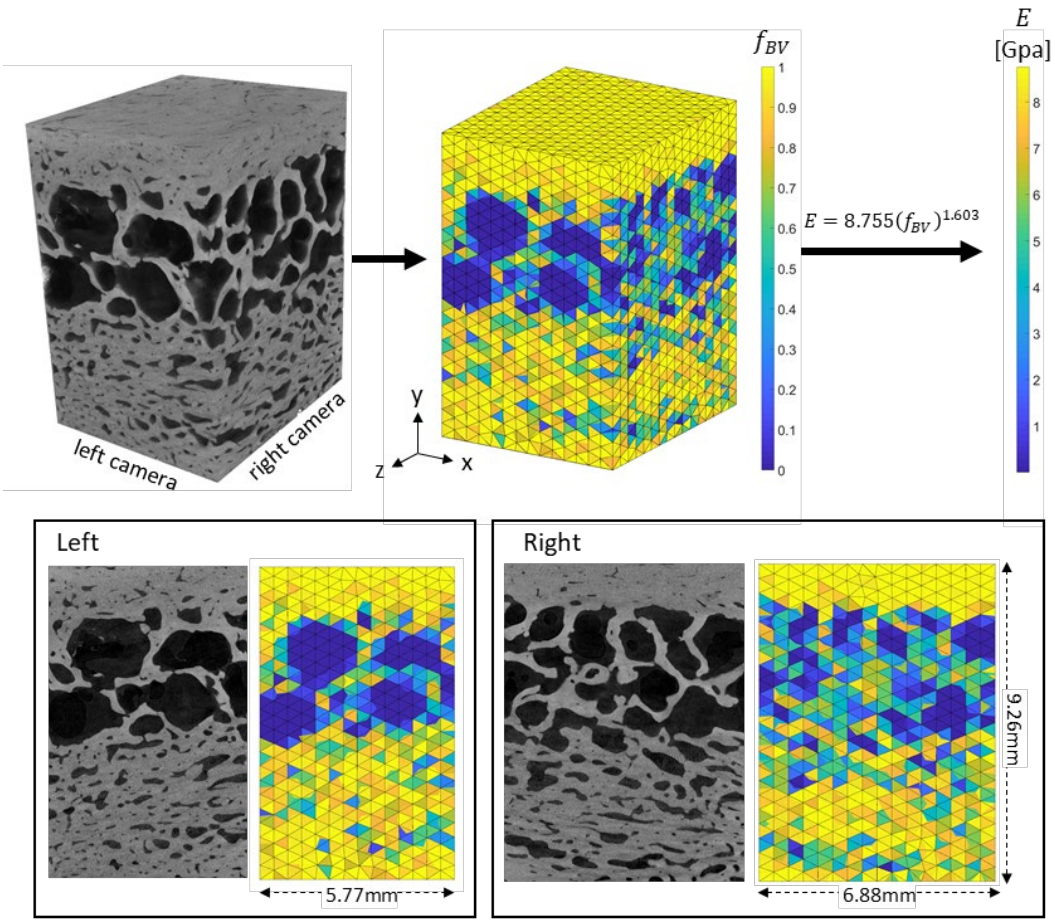

Fig. 4 Mesh of tetrahedral elements shown with rectangular portion of micro-CT images corresponding to the rectangular VOI used for mesh generation (Section 2.3); color maps of mesh elements correspond to BVF and modulus (details shown for sides facing left and right cameras in the experiment)

2.5 Boundary Conditions and Simulation Execution

The vertical displacement (in the loading direction) was constrained along the bottom surface. A single node in the center of the top surface was constrained in the x and z directions. Quasi-static compression was modeled as a displacement boundary condition applied to the top surface in the y (vertical) dimension, $\delta_{sim} = 3.901 \times 10^{-2}$mm. This value of δ_{sim} was calculated to correspond to the time point in the experiment at which the platens had displaced by δ_{exp} by accounting for the initial toe displacement in the experimental loading curve: $\delta_{sim} = \delta_{exp} - \delta_{toe}$ (see Fig. 2, Section 2.2). The simulation was executed in Abaqus/Standard 6.12 using High Performance Computing systems at ARL.

3. Results

3.1 Contact Force

The specimen stiffness, K, was measured from the linear portion of the experimental load-displacement response as 12.25kN/mm (see Fig. 2). The simulated stiffness, K_{sim}, was calculated by first determining the compressive reaction force, F_R, as the sum of the nodal force in the compression (y) direction, F_y, for all of the nodes on the top surface at the end of the simulation: $F_R = 0.4782$ kN. The stiffness was then calculated by normalizing F_R by the magnitude of the applied displacement: $K_{sim} = F_R/\delta_{sim}$= 12.26kN/mm. The load-displacement response is compared between the simulation and experiment in Fig. 5.

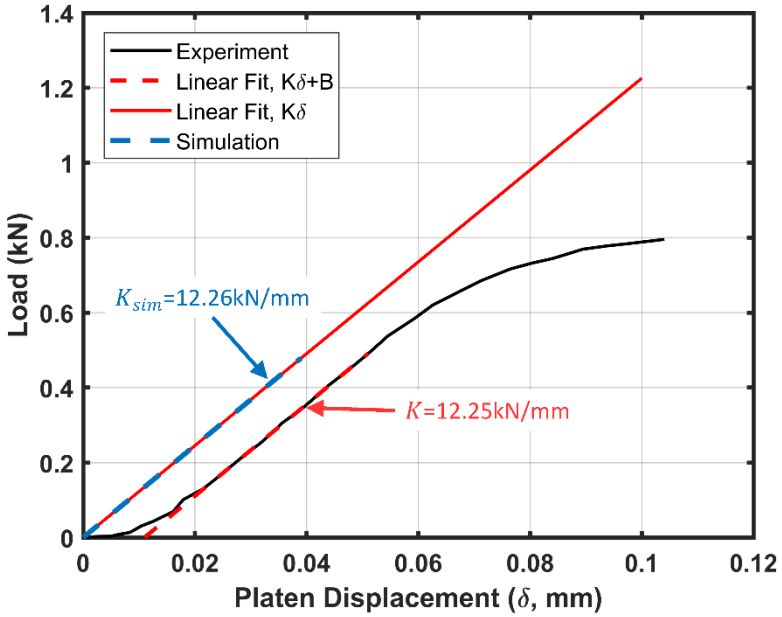

Fig. 5 Load-displacement response of the experiment and simulation; stiffness measured in linear regime of the experiment is noted as K and stiffness in the simulation is noted as K_{sim}

3.2 Strain Distribution

The 2-D strain distributions across the two faces captured by the left and right cameras were also compared between the experiment and simulation. The experimental distribution of the strain in the loading direction, ε_{yy}, was extracted from the DIC analysis of the speckled images of the left and right cameras at an applied platen displacement of $\delta_{exp} = 0.05$ mm. Then, the portion of the strain field over the particular x–y and z–y space corresponding to the rectangular VOI used for meshing, which was smaller than the full experimental specimen (Section 2.3), was compared to that of the simulation at $\delta_{sim} = 3.901 \times 10^{-2}$ mm.

These strain distributions from the experiment and simulation are shown in Fig. 6. In Fig. 6, the experimental strains are plotted over the speckled images from the cameras, which have been cropped in the horizontal dimensions (x and z for the left and right cameras, respectively) in order to correspond to the rectangular VOI. There are strain data missing for an elliptical region in the upper left quadrant of the image of the left camera due to the presence of a large pore in this region of the specimen. This pore was not completely covered with the spray-painted speckle pattern, which is required for DIC. Therefore, the region lacking the speckle pattern was avoided in the DIC analysis, and no displacement or strain data were returned for it.

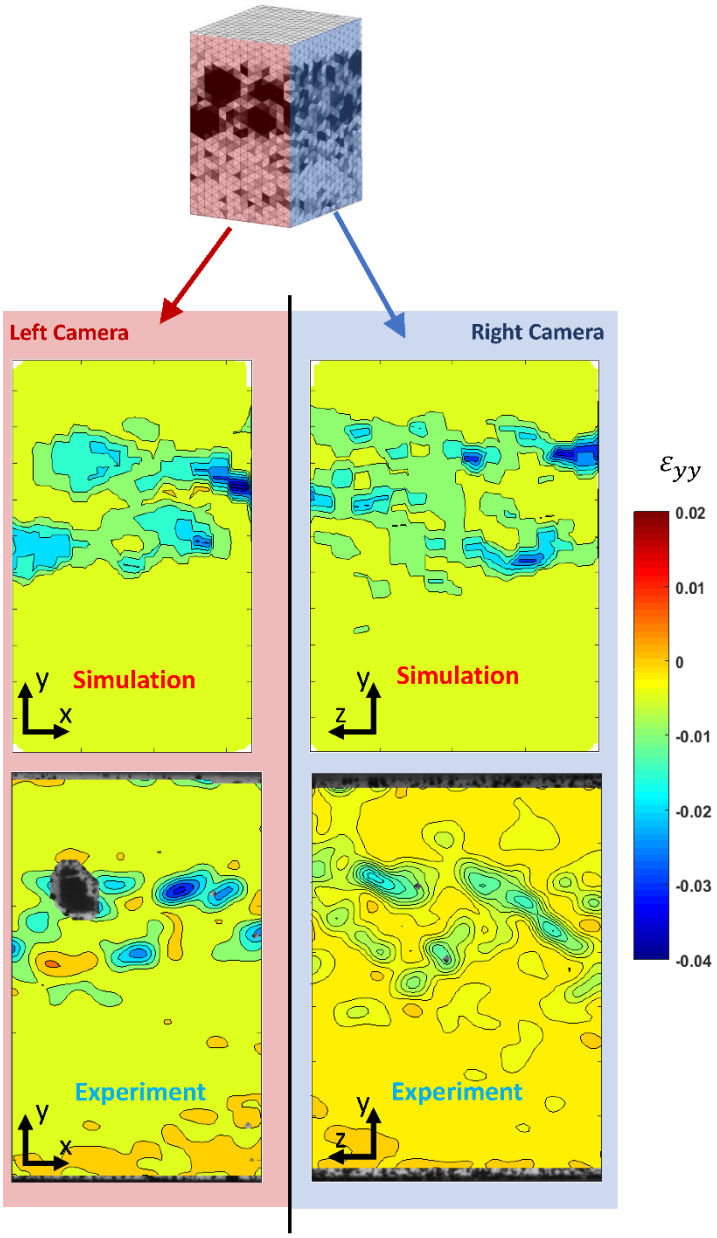

Fig. 6 Strain in the compression direction, ε_{yy}; contours are compared between the experiment at $\delta_{exp} = 0.05$ (bottom row) and simulation at $\delta_{sim} = 3.901 \times 10^{-2}$ mm (top row); for experiment and simulation, left and right camera faces are shown (Fig 4). Simulation contours are from full left and right faces of the mesh; experimental contours are limited to the rectangular portion of specimen used for mesh generation (rectangular VOI). Experimental contours are overlaid on images of speckle pattern used for DIC and are cropped in x and z dimensions, corresponding to the area of the rectangular VOI, and do not show the entire x and z dimensions of the specimen.

4. Discussion

4.1 Comparison between Simulation and Experiment

The simulation matched the initial linear loading phase of the experiment using the previously reported power-law relationship between the elastic modulus and the BVF for the human skull. The experiment was compared to the simulation by accounting for the initial toe response, which was originally indicated to arise from experimental artifacts (Alexander et al. 2018). The typical initial toe response has also been reported in other studies of the through-thickness mechanical response of human skull (Boruah et al. 2013, Motherway et al. 2009). The stiffness of the present simulation deviated from the stiffness calculated from the linear portion of the experiment by less than 0.5%.

Similarly, the 2-D compressive strain field of the simulation was comparable to that of the experiment at a time point within the linear regime of the compressive response. In both the simulation and experiment, strain was concentrated at regions of low BVF within the diploe. The magnitudes of these strain concentrations were similar, falling between $-0.015 < \varepsilon_{yy} < -0.03$.

However, there were differences in the 2-D variation in ε_{yy} between the simulation and the experiment. Most remarkably, there were noticeable regions of tensile strain ($\varepsilon_{yy} \geq 0$) in the experimental contours, which were not evident in the simulation. This key difference likely arose from representing the more complex architecture of the bone microstructure of the actual specimen as a homogenized element within the simulation mesh. Complex microstructure within an element could lead to local tensile strains. If a closer match was desired, an FE analysis could be performed using the full representation of the detailed microstructure.

4.2 Stress Distribution within the Specimen

A key assumption used to derive the power-law relationship in the previous report was that the compressive response of the specimen could be modeled as a stack of 10 layers with flat and parallel boundaries acting in series (Alexander et al. 2018). Therefore, the compressive stress σ_{yy} at any given time point during the experiment was assumed to be uniform throughout the specimen, such that σ_{yy} was invariant with respect to x, y, and z. This assumption was recognized as a gross approximation but was originally inspired from an earlier study on the compressive response of adolescent minipig skulls (Alexander et al. 2016). In that study, the compressive strain contours on the minipig skulls showed banding in the depth dimension, from the inner to outer surfaces. The strain appeared much more

strongly dependent on the depth than on the other two dimensions. However, the human skulls did not show similar prominent strain banding, and so the applicability of the constant stress assumption remained unknown as the variation in stress could not be measured experimentally.

The simulation of the present paper provided a way to evaluate the uniform stress assumption, since it was a more realistic representation of the actual specimen. Specifically, in the 10-layer model used to derive the power law from the experiment, the BVF was assumed to be constant within each of the 10 layers, whereas in the present simulation, the BVF changed element by element. To analyze whether the compressive stress σ_{yy} was uniform in the simulation, first, the minimum principal stress (σ_{min}) was extracted at the centroid of each element after the final time step, at an applied displacement of $\delta_{sim} = 3.901{\times}10^{-2}$ mm. The variation of this stress as a function of depth, $\sigma_{min}(y)$, was then obtained by sorting the stresses by the y-coordinate of the incenter of the element. Next, the depth was divided into 10 equally thick layers, in imitation of the model (Alexander et al. 2018), and $\sigma_{min}(y)$ was averaged over each of these layers (Fig. 7). In Fig. 7, the standard deviation indicates the total amount of variation of σ_{min} in the x,y, and z dimensions within the layer. Furthermore, the variation of σ_{min} with depth was compared with the far-field calculation (red line, Fig. 7) obtained by normalizing the resultant force along the top surface (F_R, Section 3.1) by the cross-sectional area of the mesh.

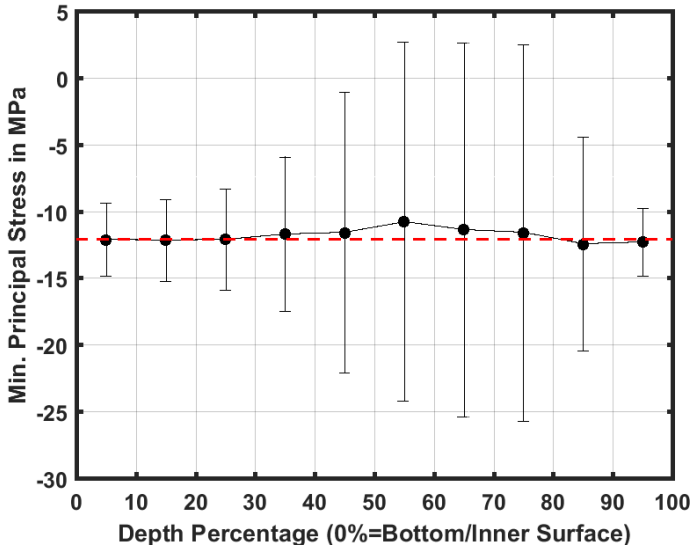

Fig. 7 Variation with depth of minimum principal stress of elements (mean ± 1 standard deviation) at the end of the simulation. Depth was divided into 10 equally thick layers; red dashed line indicates far-field stress calculated by normalizing resultant force by the cross sectional area of the mesh.

The stress showed some variation within the layers, as was expected from the heterogeneity of the simulation. The greatest amount of variation occurred in the layers corresponding to the highly porous diploe. This was likely due to the large pores in this area. The presence of large pores meant a larger proportion of elements had lower BVF values. On the other hand, in the tables, where the pores were smaller, the variation in the BVF and modulus values was also lower since most of the elements were almost entirely bone. However, despite the large variation in each layer, the average of the minimum principal stresses in each layer closely matched the far-field calculation, even in the diploe.

5. Conclusion

The power-law relationship between the BVF and modulus in the human skull, previously developed at ARL, was implemented in a FE simulation of quasi-static compression using a coarse mesh without microstructural details. A method was developed to map the FE mesh to the micro-CT data set, so as to determine the BVF of the physical space within the human skull that the element represented. This method allowed individual mechanical properties to be assigned to each element based on the BVF of the element. The stiffness calculated from the simulation closely matched the stiffness in the linear portion of the experimental response. The 2-D strain fields were also qualitatively similar even though there were localized regions of small tensile strains in the experiment, most probably due to complex local microstructural details.

Through element-specific mechanical-property assignment, and by using morphology-based mechanical properties specific to the human skull, the FE simulation of the current paper was able to match the initial linear response of the experimental mechanical response despite the simplicity of the mesh and the procedure, which lacked any microstructural details. Therefore, this simulation provided an efficient method of implementing a microstructurally informed model of the mechanical response of bones in a FE simulation using a coarser mesh, but lacking complex microstructural details, thus allowing us to bridge scales between complexity and efficiency. With the power-law relationship demonstrated to match the linear portion of the experimental results, future efforts are aimed at applying the power law to skull experiments at length scales larger than those of the coupon used in the present report. Furthermore, the model is currently being extended to also match the nonlinearity of the experiment exhibited in the load-displacement curve after the initial linear regime (see Fig. 2) by including BVF-specific failure criteria.

6. References

Alexander SL, Gunnarsson CA, Weerasooriya T. Structural influence on the mechanical response of adolescent Göttingen porcine cranial bone. Aberdeen Proving Ground (MD): Army Research Laboratory (US); 2016 Oct. Report No.: ARL-TR-7845.

Alexander SL, Gunnarsson CA, Rafaels K, Weerasooriya T. Microstructural dependence of the compressive mechanical response of human skull. Aberdeen Proving Ground (MD): Army Research Laboratory (US); 2018 Sep. Report No.: ARL-TR-8512.

Alexander SL, Rafaels K, Gunnarsson CA, Weerasooriya T. Structural analysis of the frontal and parietal bones of the human skull. J Mech Beh Biomed Mat. 2019;90(90):689–701.

Bessho M, Ohnishi I, Matsuyama J, Matsumoto T, Imai K, Nakamura K. Prediction of strength and strain of the proximal femur by a CT-based finite element method. J Biomech. 2007;40(8):1745–1753.

Boruah S, Henderson K, Subit D, Salzar R, Shender B, Paskoff G. Response of human skull bone to dynamic compressive loading. In: Proceedings of the International Research Council on Biomechanics of Injury (IRCOBI) Conference; 2013 Sep 11–13; Gothenburg, Sweden. Vol. 13; p. 497.

Boruah S, Subit DL, Paskoff GR, Shender BS, Crandall JR, Salzar RS. Influence of bone microstructure on the mechanical properties of skull cortical bone—a combined experimental and computational approach. J Mech Beh Biomed Mat. 2017;65:688–704.

Brown KR, Tarsuslugil S, Wijayathunga VN, Wilcox RK. Comparative finite-element analysis: a single computational modelling method can estimate the mechanical properties of porcine and human vertebrae. J The Royal Soc Interface. 2014;11(95):20140186.

Cook RB, Zioupos P. The fracture toughness of cancellous bone. J Biomech. 2009;42(13):2054–2060.

Fagan BT. Large-scale simulation of the mechanical response of porcine cranial bone [master's thesis]. [Cambridge (MA)]: Massachusetts Institute of Technology; 2017.

Mirzaali MJ, Schwiedrzik JJ, Thaiwichai S, Best JP, Michler J, Zysset PK, Wolfram U. Mechanical properties of cortical bone and their relationships with age, gender, composition and microindentation properties in the elderly. Bone. 2016;93:196–211.

Morgan EF, Keaveny TM. Dependence of yield strain of human trabecular bone on anatomic site. J Biomech. 2001;34(5):569–577.

Morgan EF, Bayraktar HH, Keaveny TM. Trabecular bone modulus density relationships depend on anatomic site. J Biomech. 2003;36(7):897–904.

Motherway JA, Verschueren P, Van der Perre G, Vander Sloten J, Gilchrist MD. The mechanical properties of cranial bone: the effect of loading rate and cranial sampling position. J Biomech. 2009 Sep 18;42(13):2129–2135.

Otsu N. A threshold selection method from gray-level histograms. Automatica. 1975;11(285–296):23–27.

Taddei F, Schileo E, Helgason B, Cristofolini L, Viceconti M. The material mapping strategy influences the accuracy of CT-based finite element models of bones: an evaluation against experimental measurements. Med Eng Phys. 2007;29(9):973–979.

Zhang X, Xu C, Wen Y, Luo S. The experimental and numerical study of indirect effect of a rifle bullet on the bone. Foren Sci Int. 2015;257:473–480.

List of Symbols, Abbreviations, and Acronyms

2-D	two-dimensional
3-D	three-dimensional
ARL	Army Research Laboratory
BVF	bone volume fraction
CCDC	Combat Capabilities Development Command
DIC	digital image correlation
FE	finite element
micro-CT	microcomputed tomography
RDECOM	Research, Development, and Engineering Command
STL	stereo-lithography
VOI	volume of interest

1 (PDF) DEFENSE TECHNICAL INFORMATION CTR DTIC OCA

2 (PDF) DIR ARL IMAL HRA RECORDS MGMT FCDD RLD CL TECH LIB

1 (PDF) GOVT PRINTG OFC A MALHOTRA

10 (PDF) CCDC NATICK SOLDIER SYSTEMS CTR M G CARBONI D COLANTO R DILLALLA J FONTECCHIO B KIMBALL J KIREJCZYK J PARKER M MAFEO M MARKEY D PHELPS

2 (PDF) PROG EXECUTIVE OFC SOLDIER A FOURNIER J MULLENIX

1 (PDF) MTRL SCIENCES DIV LAWRENCE BERKELY NATL LAB R RITCHIE

5 (PDF) SOUTHWEST RSRCH INST C ANDERSON JR S CHOCRON D NICOLELLA T HOLMQUIST G JOHNSON

1 (PDF) INST FOR DEFNS ANLYS Y MACHERET

4 (PDF) MRMC DOD BLAST INJURY RSRCH PRGM COOR OFC R GUPTA M LEGGIERI T PIEHLER R SHOGE

2 (PDF) MRMC JTAPIC PRGM OFC W LEI J USCILOWICZ

1 (PDF) WIAMAN PMO S MARSH

4 (PDF) US ARMY AEROMEDICAL RSRCH LAB F BROZOSKI V CHANCEY B MCENTYRE D WISE

1 (PDF) CCDC GROUND VEHICLE SYSTEMS CTR R SCHERER

1 (PDF) CCDC AMSRD PE D RUSIN

2 (PDF) CCDC CHEML BIOL CTR M HORSMON N VINCELLI

1 (PDF) OSD DOT&E J IVANCIK

5 (PDF) US NAVAL RSRCH LAB A BAGCHI A ILIOPOULOS J MICHOPOULOS K TEFERRA X TAN

3 (PDF) WHITING SCHOOL OF ENGRNG JOHNS HOPKINS UNIV T D NGUYEN B NOTGHI S BAILOOR

1 (PDF) COULTER DEPARTMENT OF BIOMEDICAL ENGRNG GEORGIA INSTITUTE OF TECHNOLOGY S MARGULIES

1 (PDF) DEPT OF ENGRNG SCI AND MECHANICS VIRGINIA POLYTECHNIC INST AND STATE UNIV R BATRA

2 (PDF) MASSACHUSETTS INST OF TECHLGY
INST FOR SOLDIER NANOTECHNOLOGIES
R RADOVITZKY
S SOCRATE

1 (PDF) DEPT OF MECHL AND NUCLEAR ENGRNG
THE PENNSYLVANIA STATE UNIV
R KRAFT

1 (PDF) INDIAN INST OF TECH
R BHARDWAJ

1 (PDF) CENTER FOR APPLIED BIOMECHANICS
UNIVERSITY OF VIRGINIA
R SALZAR

85 (PDF) DIR ARL
FCDD DAS LA
P BAKER
FCDD DAS LBE
J GURGANUS
FCDD DAS LBW
G DIETRICH
W MERMAGEN
S SNEAD
FCDD RLC HC
E CHIN
FCDD RLC NS
R CARTER
FCDD RLD P
S WALSH
FCDD RLW
S KARNA
A RAWLETT
S SCHOENFELD
FCDD RLW L
W OBERLE
FCDD RLW LF
G BROWN
FCDD RLW LH
T EHLERS
L MAGNESS
C MEYER
J NEWILL
D SCHEFFLER
B SCHUSTER
FCDD RLW M
J BEATTY
B LOVE
J MCCAULEY
J SINGH
FCDD RLW MA
J LA SCALA
D O'BRIEN
T PLAISTED
J STANISZEWSKI
K STRAWHECKER
E WETZEL
C YEN
FCDD RLW MB
G GAZONAS
D GRAY
P MOY
B POWERS
T WALTER
V WU
FCDD RLW MC
R JENSEN
FCDD RLW MD
A BUJANDA
B CHEESEMAN
J SOUTH
J SIETINS
FCDD RLW ME
J LASALVIA
P PATEL
J SWAB
L VARGAS-GONZALEZ
FCDD RLW MF
B DOWDING
S GRENDAHL
FCDD RLW MG
J LENHART
K MASSER
R MROZEK
FCDD RLW PA
S BILYK
FCDD RLW PB
S ALEXANDER
A BROWN
A DAGRO
A DILEONARDI
A EIDSMORE
B FAGAN
A GUNNARSSON
C HAMPTON
C HOPPEL
M KLEINBERGER
E MATHEIS
J MCDONALD
P MCKEE
K RAFAELS
S SATAPATHY
M SCHEIDLER
K THOMPSON
T WEERASOORIYA
S WOZNIAK

T ZHANG
FCDD RLW PC
R BECKER
J BRADLEY
D CASEM
C MEREDITH
A SOKOLOW
FCDD RLW PD
R DONEY
C RANDOW
FCDD RLW PE
M BURKINS
P GILLICH
M LOVE
P SWOBODA
FCDD RLW PF
N GNIAZDOWSKI
R GUPTA